Electrochemical Materials and Technologies

ARTICLE

eISSN: 2949-0561

Cite this: Electrochem. Mater. Technol. 4 (2025) 20254051

Oxygen-ionic transport in the novel Ca-doped complex oxides based on $BaLaInO_4$

Natalia Tarasova [a]*, Ekaterina Abakumova [a], Tamara Kuznetsova [a]

Received: 11 March 2025
Accepted: 3 April 2025
Published online: 10 April 2025

DOI: 10.15826/elmattech.2025.4.051

Electrochemical energy sources are part of the new energy sector due to their high efficiency and cost effectiveness. Solid oxide fuel cells are an excellent example of these devices. They are made from a variety of materials, including ceramics. Oxygen ion conductive ceramics can be used as the electrolyte material. In this work, the isovalent doping of the barium sublattice by calcium ions has been carried out for the first time. The effect of doping on the structure and electrical conductivity was investigated. Doping leads to an increase in conductivity values compared to the matrix composition. The greatest increase in conductivity was observed for the composition with low dopant concentration.

keywords: $BaLaInO_4$, layered perovskite, Ruddlesden-Popper structure, oxygen-ionic conductivity

1. Introduction

One of the most important problems of the 21st century is the threat of global warming due to the large amount of CO_2 emissions from energy production from fossil fuels [1–4]. The development of environmentally friendly and resource-saving hydrogen energy can help solve the environmental problem. The environmentally friendly energy sources are fuel cells, which are an electrochemical current source that works by converting the energy of chemical reactions of the fuel into electrical energy. This is very promising both from the point of view of the availability of energy resources and from the point of view of environmental protection [5–9].

There are several types of fuel cells used in hydrogen energy. Fuel cells, for example, can be classified according to their operating principle and the type of electrolyte material used. There are fuel cells with a polymer-electrolytic membrane (PEMFC), solid oxide fuel cells (SOFC), alkaline fuel cells (AFC), phosphoric acid fuel cells (PAFC) and fuel cells with molten carbonate (MCFC) [10–11]. Solid-state electrolytes (SSE) are a promising class of energetic materials in which specific groups of ions can be induced to diffuse through a crystalline matrix. Solid electrolytes have a number of advantages, including non-flammability and high thermal and chemical stability. SE form the basis for clean energy conversion and storage technologies such as fuel cells, electrocatalysts, and solid-state batteries. Therefore, optimizing their ion transport properties is crucial for energy and sustainable development.

As a result, SOFCs have a number of advantages over other types of fuel cells, including 60–80 % higher conversion efficiency, longer lifetime, etc. [12]. At the same time, when using SOFC, fewer pollutants are released into the environment, and they do not require catalysis by precious metals. SOFCs can operate on various types of fuel, such as hydrocarbons, coal gas, biomass, hydrogen, and synthesis gas [13]. While SOFCs are independent of pure hydrogen supplies, since hydrocarbons can be fed into the fuel cell and converted

a: Institute of High-Temperature Electrochemistry UB RAS, Ekaterinburg 620066, Russia

* Corresponding author: Natalia.Tarasova@ihte.ru

into a hydrogen-rich stream through internal thermochemical processes [13, 14]. The study of solid oxide fuel cells requires the synthesis and study of new materials with oxygen-ion and proton properties. Complex $BaLaInO_4$-based oxides with high ionic conductivity values can be used as electrolytes in SOFCs.

Materials with a perovskite structure characterized by the general formula ABO_3 receive a significant share of attention for use as SOFC conductors [15, 16]. However, new classes of ionic conductors with a perovskite-related structure, such as perovskite-$BaLaInO_4$ layered materials [17–20], are attracting increasing attention. In contrast to classical perovskites, layered RP-structures have a space between the layers. Due to this structural characteristic, layered perovskites need to be studied more intensively. The compositions $Ba_{1-x}Ca_xLaInO_4$ (x = 0.05, 0.1, 0.15) were obtained. The effect of doping on the structure and electrical conductivity was investigated.

2. Experimental

The solid solution $Ba_{1-x}Ca_xLaInO_4$ (x = 0, 0.05, 0.1 and 0.15) was obtained by thoroughly grinding La_2O_3, In_2O_3, $BaCO_3$ and $CaCO_3$ in an agate mortar according to the stoichiometric coefficients. The weighed portions of pre-dried oxides and carbonates powders were taken on a Sartorius ACCULAB ALC-210d4 analytical scale (Sartorius Weighing Technology GmbH, Germany). The powder blends were annealed in a Nabertherm furnace after grinding. The initial annealing temperature was set at 800 °C. The total annealing range was 800–1300 °C. The chemical reaction according to the stoichiometric coefficients led to the solid solution $Ba_{1-x}Ca_xLaInO_4$ (x = 0, 0.05, 0.1 and 0.15):

$$(1-x)BaCO_3 + 0.5La_2O_3 + 0.5In_2O_3 + \\ + xCaCO_3 \longrightarrow Ba_{1-x}Ca_xLaInO_4 + CO_2\uparrow. \quad (1)$$

The phase composition was controlled by X-ray phase analysis using a Bruker Advance D8 diffractometer (Bruker, Billerica, MA, USA). The parameters for the X-ray were a step of 0.01 ° and a speed of 0.5 °/min. XRD measurements were carried out at a controlled room temperature. In order to investigate the new solid solution $Ba_{1-x}Ca_xLaInO_4$, a structure refinement was carried out by means of the Rietveld method. The Rietveld method was carried out in the FullProf program. Calculation of bond lengths, analysis and visualization of the structure are performed in the VESTA program.

The morphology of the solid-phase solution $Ba_{1-x}Ca_xLaInO_4$ (x = 0.05, 0.1, 0.15) on the sintered tablets was studied using a Vega 3 Tescan scanning electron microscope (SEM) coupled with an energy-dispersive X-ray spectroscopy (EDS) system.

The conductivity of the compositions $Ba_{1-x}Ca_xLaInO_4$ (x = 0, 0.05, 0.1 and 0.15) was measured using a Z-1000P impedance-meter (Elins, Russia). Frequencies were in the range of 100 Hz to 1 MHz. Bulk resistance was calculated from impedance spectra using Zview software fitting (Scribner Associates Inc., Southern Pines, NC). For this measurement, a 10 mm diameter tablet was sintered at a temperature of 1300 °C for 24 hours. Platinum paste was used as electrodes and applied in a thin layer on the tablet. The platinum electrodes were annealed at 1000 °C for 3 hours. The investigations were carried out from 1000 to 200 °C with a cooling rate of 1 °/min under dry air or dry Ar. The dry gas (air or Ar) was prepared by circulating the gas through P_2O_5 ($pH_2O = 3.5 \cdot 10^{-5}$ atm).

3. Results and discussions

Phase attestation of solid solution $Ba_{1-x}Ca_xLaInO_4$ carried out using the XRD method. It was shown that the compositions at dopant concentrations $0 \le x \le 0.15$ were single phase and belonged to the space group $I4/mmm$ (tetragonal symmetry). XRD patterns of $Ba_{0.9}Ca_{0.1}LaInO_4$ composition are presented in Figure 1. In contrast, the matrix composition $BaLaInO_4$ has orthorhombic symmetry (*Pbca* space group). It is obvious that the introduction of the dopant led to a change in the local structure and an increase in the symmetry. However, in order to gain a more accurate understanding of the effect of doping on the structure, a structural analysis of the samples was carried out and the bond lengths were determined. As can be seen from Figure 2, the $Ba_{0.9}Ca_{0.1}LaInO_4$ sintered sample is a densely packed round agglomerates of 20–40-micron particles. The lattice parameters and unit cell volume for the compositions are presented in Table 1. Table 2 shows the bond length values for the compositions. *R*-factors for the new solid solution $Ba_{1-x}Ca_xLaInO_4$ are shown in Table 3. As can be seen, doping with smaller ionic radii ($r_{Ba^{2+}}$ = 1.47 Å; $r_{Ca^{2+}}$ = 1.18 Å [21]) leads to the decrease in the lattice parameters. However, the redistribution of bond lengths occurs in a more complex manner. The average bond length <Ba/Ca/La–O> decreases with the introduction of the dopant and continues to decrease as its concentration increases. The average bond length <In–O> also decreases with the introduction of calcium, but an increase in calcium concentration leads to an increase in this bond length. It is obvious that such a redistribution of bond lengths ultimately leads to a change in the tilt angle of the polyhedra and a general increase in the symmetry of the structure. The possible reason for these changes is the appearance of different

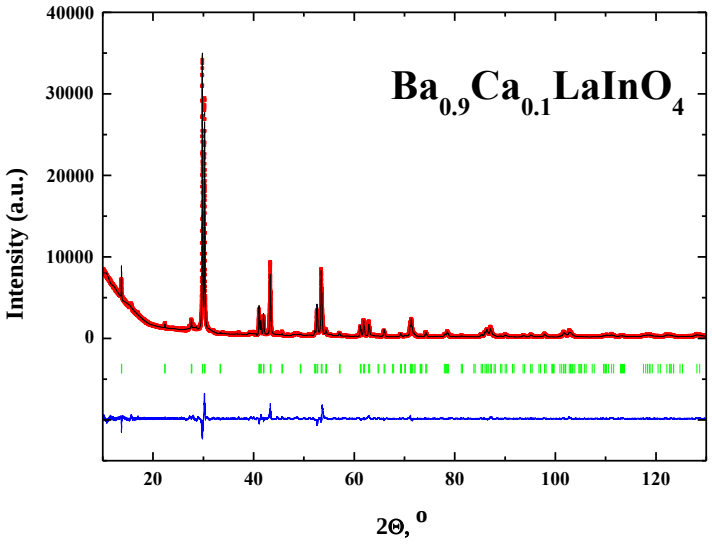

Figure 1 Refinement of the XRD for the composition $Ba_{0.9}Ca_{0.1}LaInO_4$.

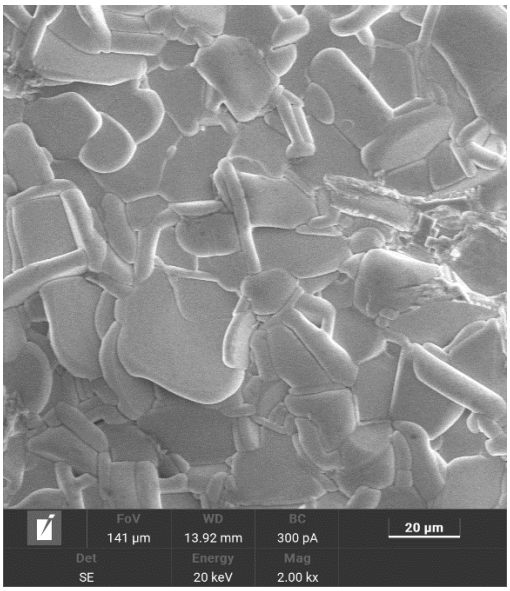

Figure 2 SEM image of the $Ba_{0.9}Ca_{0.1}LaInO_4$ ceramic sample.

Table 1 – The lattice parameters and unit cell volume for obtained compositions.

Lattice parameters	$BaLaInO_4$	$Ba_{0.95}Ca_{0.05}LaInO_4$	$Ba_{0.9}Ca_{0.1}LaInO_4$	$Ba_{0.85}Ca_{0.15}LaInO_4$
a, Å	12.932(3)	4.176(6)	4.175(7)	4.174(6)
b, Å	5.906(0)	4.176(6)	4.175(7)	4.174(6)
c, Å	5.894(2)	12.925(3)	12.907(7)	12.889(1)
V, Å^3	450.19(5)	225.470(9)	225.07(4)	224.63(1)

Table 2 – The bond lengths values for obtained compositions.

Bond lengths (Å)	$BaLaInO_4$	$Ba_{0.95}Ca_{0.05}LaInO_4$	$Ba_{0.9}Ca_{0.1}LaInO_4$	$Ba_{0.85}Ca_{0.15}LaInO_4$
<Ba/Ca/La–O1>	2.815(2)	2.800(1)	2.796(3)	2.796(8)
<Ba/Ca/La–O2>	2.864(0)	2.433(2)	2.383(4)	2.303(4)
<Ba/Ca/La–O>	2.839(6)	2.616(6)	2.589(8)	2.550(1)
<In–O1>	2.141(3)	2.088(3)	2.087(9)	2.087(3)
<In–O2>	2.180(2)	2.164(1)	2.210(3)	2.279(6)
<In–O>	2.162(2)	2.126(2)	2.149(1)	2.183(4)

Table 3 – *R*-factors for the new solid solution $Ba_{1-x}Ca_xLaInO_4$.

R-factors	$Ba_{0.95}Ca_{0.05}LaInO_4$	$Ba_{0.9}Ca_{0.1}LaInO_4$	$Ba_{0.85}Ca_{0.15}LaInO_4$
Chi2	2.13	2.96	2.70
Rp	4.3	5.0	4.6
Rwp	3.4	3.7	3.0
Rexp	4.02	4.70	4.04
Chi2 (Bragg contrib.)	2.122	2.731	2.67
Bragg *R*-factor	2.031	2.64	2.91

natural ions in the cationic sublattice ($Ca^{2+} \rightarrow Ba^{2+}$).

The electrical conductivity values were obtained using the impedance spectroscopy method in the atmospheres with controlled humidity (pH_2O) and oxygen partial pressure (pO_2). The Nyquist plots are shown in Figures 3 for the composition $Ba_{0.9}Ca_{0.1}LaInO_4$ as an example of typical plots. All obtained Nyquist plots contain two semicircles (Figure 3 a). The small semicircle starting from zero coordinates (high-frequency semicircle) corresponds to the resistivity of the grain volume of polycrystalline sample.

This is proven by the small capacitance value ~ 10^{-12} F/cm. The large semicircle (low frequency semicircle) corresponds to the resistivity of the grain boundaries with a capacitance value ~ 10^{-9} F/cm. The conductivities were calculated from the resistivity values

taken at the intersection of the high-frequency semicircle with the abscissa axis. The influence of temperature and oxygen partial pressure on the Nyquist plot is shown in Figures 3 b and 3 c respectively. The temperature dependencies of the conductivity obtained under dry air (pO_2 = 0.21 atm) and dry Ar (pO_2 ~ 10^{-5} atm) are shown in Figure 4. As can be seen, the introduction of calcium ions into the barium sublattice leads to an increase in the conductivity values compared to the matrix composition.

The comparison of the conductivity values obtained under dry air and dry Ar conditions (Figure 5) shows the changes in the proportion of oxygen-ionic transport with varying temperature and calcium concentration. The conductivity nature under dry Ar (i.e. at lower oxygen partial pressure) is predominantly oxygen-ionic. The proportion of oxygen transport (oxygen-ion transport numbers) is defined as the ratio of oxygen-ion conductivity to total conductivity:

$$t_{O^{2-}} = \frac{\sigma^{Ar}}{\sigma^{air}}. \quad (2)$$

At the high temperature (900 °C), the oxygen ionic transport numbers are the same for all Ca-doped compositions and are ~ 40 %. As the temperature decreases, the values of the oxygen ionic transport numbers change. They increase up to ~ 60 % for the composition with x = 0.05 and decrease up to ~ 20 % for the compositions with x = 0.10 and 0.15. The oxygen ionic transport numbers are ~ 20 % over the whole temperature range.

The fact that the values of the oxygen ionic transport coefficients change with the variation of the calcium content is very interesting. Calcium doping of the barium sublattice does not lead to the formation of oxygen defects in the anionic sublattice. Instead, fragments Ba–O–Ca (at "low" doping concentrations) and Ca–O–Ca (at "high" doping concentrations) appear in the structure at the sites of the matrix fragment Ba–O–Ba.

It can be assumed that the transport of oxygen is facilitated in the case of its bonding with atoms of different nature Ba–O–Ca, which leads to an increase in the ionic component of the conductivity (case of composition with x = 0.05) due to the increase in the proportion of mobile oxygen ions. An increase in calcium concentration can lead to the appearance of Ca–O–Ca fragments in the structure and to a decrease in oxygen transport.

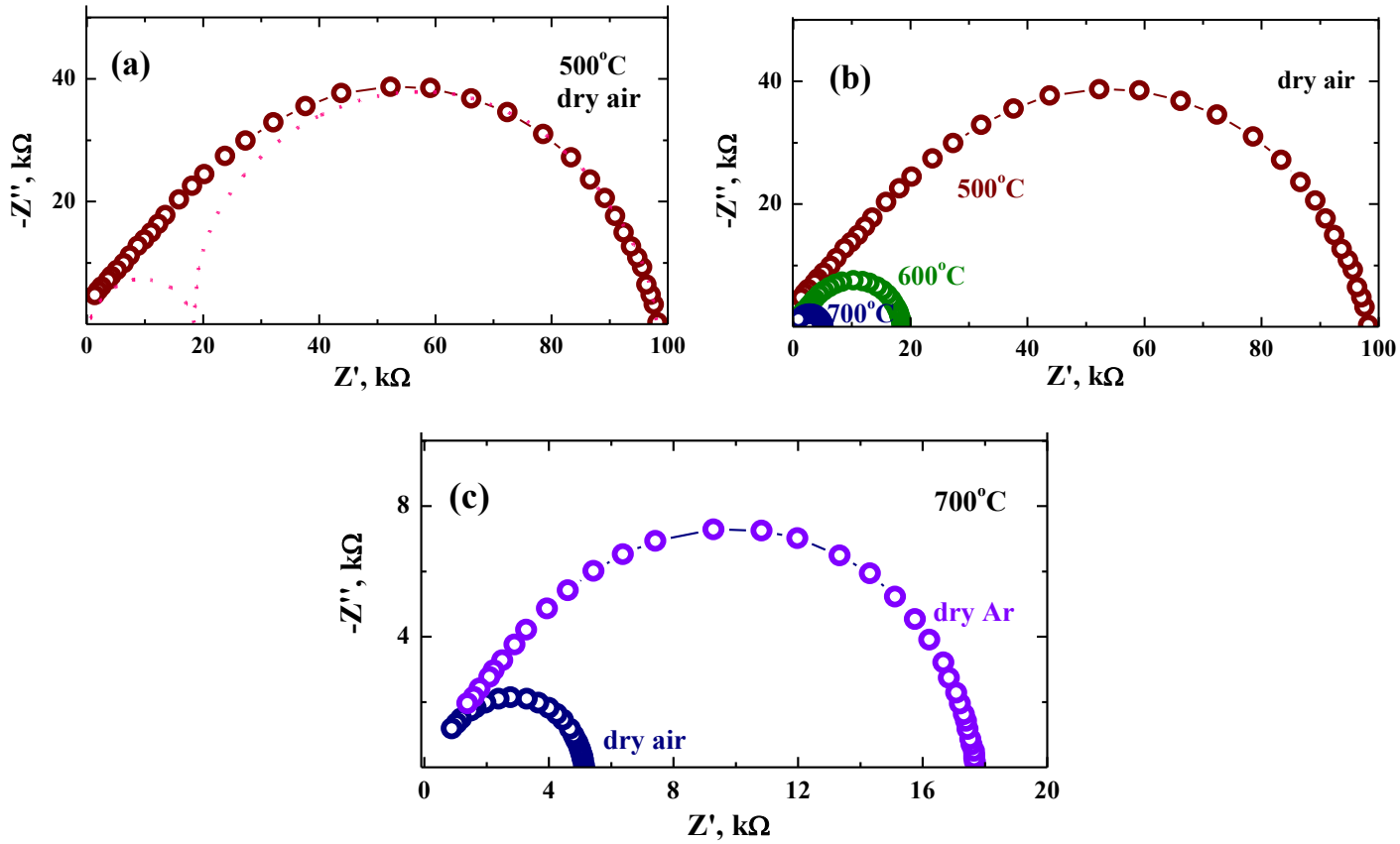

Figure 3 The Nyquist plots for the composition $Ba_{0.9}Ca_{0.1}LaInO_4$ obtained at 500 °C in dry air (a), at 500, 600 and 700 °C in dry air (b) and at 700 °C in dry air and dry Ar (c).

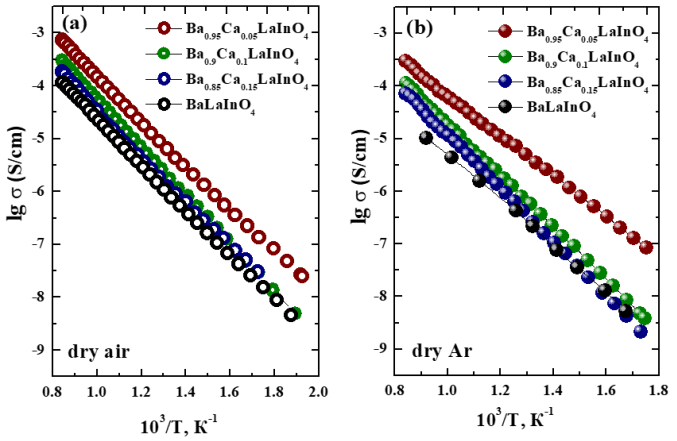

Figure 4 The temperature dependencies of conductivity for investigated compositions obtained at dry air (a) and dry Ar (b).

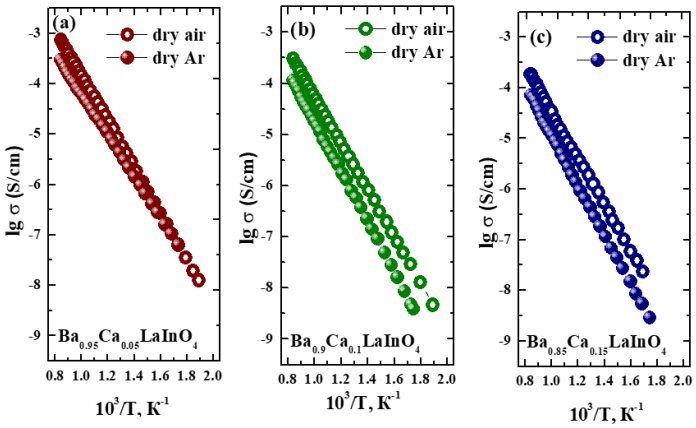

Figure 5 The temperature dependencies of conductivity for compositions $Ba_{0.95}Ca_{0.05}LaInO_4$ (a), $Ba_{0.9}Ca_{0.1}LaInO_4$ (b), $Ba_{0.85}Ca_{0.15}LaInO_4$ (c).

These considerations can also explain the concentration dependencies of the oxygen-ionic conductivity (Figure 6 a). As can be seen, calcium doping leads to an increase in conductivity values with respect to the matrix composition. At the same time, the composition with the lowest doping concentration ($x = 0.05$) has the highest conductivity values. Further increase in calcium concentration leads to a decrease in conductivity values. In other words, the "high" calcium concentration (the appearance of Ca–O–Ca fragments) is one of the possible reasons for the decrease in conductivity. However, the concentration dependence of the total conductivity, which is the sum of the ionic and electronic components of the conductivity, has the same shape (Figure 6 b).

Accordingly, increasing the dopant concentration leads to a decrease not only in the oxygen ionic conductivity but also in the total conductivity. Calcium doping is accompanied by a decrease in unit cell parameters and unit cell volume, i.e., a decrease in migration volume. Not only does the proportion of mobile oxygen ions decrease, but also the mobility of the oxygen ions as a whole also decreases.

Therefore, calcium doping of barium sublattice of layered perovskite $BaLaInO_4$ up to ~ 0.9 order of magnitude for total conductivity and up to ~ 1.5 orders of magnitude for oxygen-ionic conductivity (at low temperatures for $Ba_{0.9}Ca_{0.1}LaInO_4$ composition). The introduction of higher calcium concentrations ($x > 0.05$) leads to a decrease in both total and oxygen-ion conductivity. Figure 7 shows a comparison of Ca^{2+} doped compounds by isovalent substitution and acceptor substitution relative to undoped $BaLaInO_4$. It is clear that isovalent doping increases conductivity relative to undoped, but acceptor doping increases conductivity more significantly, as can be seen from Figure 7.

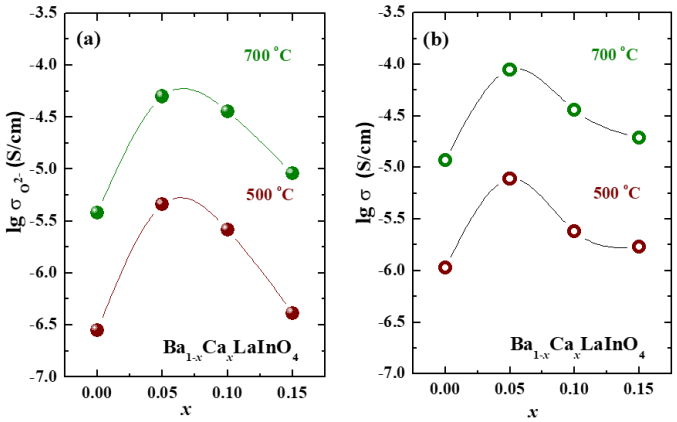

Figure 6 Concentration dependencies of oxygen-ionic (a) and total (b) conductivities.

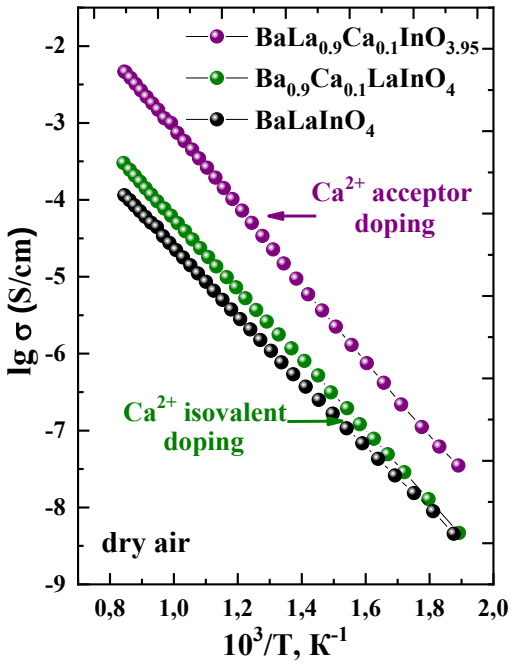

Figure 7 Comparison of compounds doped with Ca^{2+} by means of isovalent doping and acceptor doping [22] is relatively undoped $BaLaInO_4$.

From the point of view of the principles of solid state chemistry, point defects do not occur with isovalent doping. While acceptor doping creates oxygen vacancies and changes the oxygen non-stoichiometry. The quasi-chemical reaction of this process is described by Equation 3. A significant increase in conductivity due to acceptor doping can be explained by the appearance of oxygen vacancies in the structure and an increase in interlayer space, as mentioned [22]. At the same time, for isovalent doping, the increase in conductivity is only due to an increase in interlayer space, which is confirmed by the calculation of bond lengths.

$$CaO \xrightarrow{La_2O_3} 2Ca'_{La} + 2O^{\times}_{O} + V^{\bullet\bullet}_{O}. \quad (3)$$

4. Conclusions

The calcium-doped layered perovskites $Ba_{1-x}Ca_xLaInO_4$ (x = 0.05, 0.1, 0.15) were obtained for the first time. The effect of doping on the structure and electrical conductivity was investigated. Doping causes the symmetry change from *Pbca* (for matrix composition) to *I4/mmm* (for doped composition). The average bong lengths metal–oxygen decrease with the introduction of calcium. The introduction of calcium ions into barium sublattice leads to the increase in the conductivity values compared with the matrix composition. The greatest increase in conductivity (up to ~ 0.9 order of magnitude for total conductivity and up to ~ 1.5 orders of magnitude for oxygen-ionic conductivity) is observed for the composition with small dopant concentration.

Funding

This research had no external funding.

Acknowledgments

None.

Author contributions

Natalia Tarasova: Conceptualization; Funding acquisition; Methodology; Visualization; Writing – Original draft; Writing – Review & Editing.

Ekaterina Abakumova: Funding acquisition; Methodology; Visualization; Writing – Original draft.

Tamara Kuznetsova: Funding acquisition; Methodology; Visualization; Writing – Original draft.

Conflict of interest

The authors declare no conflict of interest.

Additional information

Tarasova Natalia, Orcid: 0000-0001-7800-0172; Scopus Author ID: 37047923700;

Abakumova Ekaterina, Orcid: 0000-0002-6102-6461; Scopus Author ID: 57699973300;

Kuznetsova Tamara, Orcid: 0009-0000-5062-184X; Scopus Author ID: 57752091200.

Institute's website: https://ihte.ru/?page_id=3106

Institute of High Temperature Electrochemistry of the Ural Branch of the Russian Academy of Sciences,

References

1. Shu DY, Deutz S, Winter BA, Baumgärtner N, The role of carbon capture and storage to achieve net-zero energy systems: trade-offs between economics and the environment, Ren. Sust. Ener. Rev., **178(6396)** (2023) 113246. https://doi.org/10.1016/j.rser.2023.113246

2. Davis SJ, Caldeira K, Matthews HD, Future CO_2 emissions and climate change from existing energy infrastructure, Science, **329(5997)** (2010) 1330–1333. https://doi.org/10.1126/science.1188566

3. Tyquin E, Weeks CS, Mehta A, Newton C, Delivering an energy export transition: Impact of conflicting and competing informational contexts on public acceptance of Australia's hydrogen export industry, Int. J. Hydrogen Energy, **61** (2024) 226–237. https://doi.org/10.1016/j.ijhydene.2024.02.185

4. Krause J, Yugo M, Samaras Z, Edwards S, et al., Well-to-wheels scenarios for 2050 carbon-neutral road transport in the EU, J. Clean. Prod., **443** (2024) 141084. https://doi.org/10.1016/j.jclepro.2024.141084

5. Younas M, Shafique S, Hafeez A, Javed F, et al., An overview of hydrogen production: current status, potential, and challenges, Fuel, **31615** (2022) 123317. https://doi.org/10.1016/j.fuel.2022.123317

6. Singh M, Zappa D, Comini E, Solid oxide fuel cell: Decade of progress, future perspectives and challenges, Int. J. Hydrogen Energy, **46(54)** (2021) 27643–27674. https://doi.org/10.1016/j.ijhydene.2021.06.020

7. Xu Q, Guo Z, Xia L, He Q, et al., A comprehensive review of solid oxide fuel cells operating on various promising alternative fuels, Energy Conversion and Management, **253** (2022) 115175. https://doi.org/10.1016/j.enconman.2021.115175

8. Peng J, Huang J, Wu X, Xu Y, et al., Solid oxide fuel cell (SOFC) performance evaluation, fault diagnosis and health control: A review, Journal of Power Sources, **505** (2021) 230058. https://doi.org/10.1016/j.jpowsour.2021.230058

9. Parente C, Teixeira F, Cerdeira J, 'Stakeholders' perceptions of hydrogen and reflections on energy transition governance, Energy. Sustain. Soc., **14** (2024) 1–19. https://doi.org/10.1186/s13705-023-00429-w

10. Vansh M, Siddharth S, Mudit KB, Mohit V, Comparative study and analysis between Solid Oxide Fuel Cells (SOFC) and Proton Exchange Membrane (PEM) fuel cell – A review, Materials today: Proceedings, **47(10)** (2021) 2270–2275. https://doi.org/10.1016/j.matpr.2021.04.203

11. Norby T, Widerøe M, Glöckner R, Larring Y, Hydrogen in oxides, Dalton Transactions, **19** (2004) 3012–3018. https://doi.org/10.1039/B403011G

12. Syafkeena N, Affandi M, Osman N, Short review on global trends in SOFC scenario and future perspective, Materials today: Proceedings, **66(10)** (2022) 3981–3984. https://doi.org/10.1016/j.matpr.2022.04.824

13. Kong W, Han Zh, Lu S, Gao X, A novel interconnector design of SOFC, Int. J. Hydrogen Energy, **45(39)** (2020) 20329–20338. https://doi.org/10.1016/j.ijhydene.2019.10.252

14. Sahli Y, Moussa HB, Zitouni B, Optimization study of the produced electric power by SOFCs, Int. J. Hydrogen Energy, **44(39)** (2019) 22445–22454. https://doi.org/10.1016/j.ijhydene.2018.08.162

15. Matsuzaki K, Saito K, Ikeda Y, Nambu Y, et al., High Proton Conduction in the Octahedral Layers of Fully Hydrated Hexagonal Perovskite-Related Oxides, J. Am. Chem. Soc., **146(27)** (2024) 18544–18555. https://doi.org/10.1021/jacs.4c04325

16. Fop S, Dawson JA, Fortes AD, Ritter C, McLaughlin AC, Hydration and ionic conduction mechanisms of hexagonal perovskite derivative, Chemistry of Materials, **33(12)** (2021) 4651–4660. https://doi.org/10.1021/acs.chemmater.1c01141

17. Tarasova N, Animitsa I, Galisheva A, Medvedev D, Layered and hexagonal perovskites as novel classes of proton-conducting solid electrolytes: A focus review, Electrochem. Mater. Technol., **1** (2022) 20221004. https://doi.org/10.15826/elmattech.2022.1.004

18. Tarasova N, Galisheva A, Animitsa I, Korona D, et. al., Protonic transport in layered perovskites $BaLa_nIn_nO_{3n+1}$ (n = 1, 2) with Ruddlesden-Popper structure, Appl. Sci., **12(8)** (2022) 4082. https://doi.org/10.3390/app12084082

19. Tarasova N, Animitsa I, Galisheva A, Pryakhina V, Protonic transport in the new phases $BaLaIn_{0.9}M_{0.1}O_{4.05}$ (M = Ti, Zr) with Ruddlesden-Popper structure, Solid State Sciences, **101** (2020) 106121. https://doi.org/10.1016/j.solidstatesciences.2020.106121

20. Tarasova N, Galisheva A, Animitsa I, Anokhina I, Novel mid-temperature $Y^{3+} \rightarrow In^{3+}$ doped proton conductors based on the layered perovskite $BaLaInO_4$, Ceramics International, **48(11)** (2022) 15677–15685. https://doi.org/10.1016/j.ceramint.2022.02.102

21. Shannon RD, Revised effective ionic radii and systematic studies of interatomic distances in halides and chalcogenides, Acta Cryst. A, **32** (1976) 751–767. https://doi.org/10.1107/S0567739476001551

22. Tarasova N, Galisheva A, Animitsa I, Korona D, Incorporation and conduction of protons in Ca, Sr, Ba-doped $BaLaInO_4$ with Ruddlesden-Popper structure, Materials, **12(10)** (2019) 1668–1682. https://doi.org/10.3390/ma12101668